AMS Home   Journals Home   Journal Archive   Subscribe   For Authors   Help   Advanced Search

Full Text View

Jet Structure and Scaling in Southern Ocean Models

B. Sinha

Plymouth Marine Laboratory, Citadel Hill, Plymouth, United Kingdom

K. J. Richards

Southampton Oceanography Centre, Southampton, United Kingdom

ABSTRACT

The jet structure of the Antarctic Circumpolar Current (ACC) simulated by two general circulation models (GCMs), FRAM (Fine Resolution Antarctic Model) and POP (Parallel Ocean Program), is examined in relation to the bottom topography field. Despite differences in configuration both GCMs display similar behavior: the model ACC consists of a number of distinct current cores superimposed on broader-scale flow. The jets display temporal and spatial (including vertical) coherence with maximum velocities occurring at the surface. It is shown that multiple jets can arise in wind-forced baroclinic quasigeostrophic flow. The main factors influencing the number and spacing of jets are found to be the bottom topography and the proximity of lateral boundaries. The meridional spacing of jets on a flat-bottomed β plane is consistent with the Rhines scaling criterion for barotropic β-plane turbulence with a small modification due to baroclinicity and the presence of meridional boundaries. When a zonally oriented ridge is present, the meridional spacing decreases. This is explained by postulating that the β effect is augmented by a factor related to the topographic slope. Smaller-scale roughness alters the magnitude of the mean flow and mass transport but does not necessarily alter the meridional scaling. The number and meridional spacing of multiple jets in FRAM are also found to be broadly consistent with this hypothesis, although other effects such as topographic steering may also be important. The POP model generally exhibits shorter length scales than would be expected from the topographically modified Rhines scaling alone, and it is likely that other factors are present.

Options:
- Create Reference
- Email this Article
- Add to MyArchive
- Search AMS Glossary

Search CrossRef for:
- Articles Citing This Article

Search Google Scholar for:
- B. Sinha
- K. J. Richards

1. Introduction

A well-observed feature of the Antarctic Circumpolar Current (ACC) is the zonation of the flow field. In Drake Passage this zonation takes the form of three distinct regions separated by transition zones associated with the ACC current cores (Nowlin and Klinck 1986; see also Nowlin and Clifford 1982). There is some evidence that suggests that the zonation is

circumpolar in extent, although possibly varying in the number of zones and their widths (Hofmann 1985; Orsi et al. 1995).

A banded structure in the velocity field is also seen in the results from numerical models of the Southern Ocean. The numerical solutions obtained by the Fine Resolution Antarctic Model (FRAM Group 1991) exhibit a flow structure that is dominated along the track of the ACC by elongated filaments of high velocity embedded in slower moving fluid. This is illustrated in Fig. 1 ⊙▬, a plot of the eastward component of velocity u versus depth at 270°E. The jet structure is coherent down to depths of about 1500 m. Typical velocities are $O(10 \text{ cm s}^{-1})$. The meridional scale of variation is of order a few hundred kilometers. The time dependent behavior of the multiple jets is illustrated in Fig. 2 ⊙▬, which shows a contour plot of instantaneous near-surface (32.5 m) u velocity against time and latitude (i.e., a Hovmöller diagram) at 270°E. The flow consists of a number of jets correlated over time and space. The jets meander to the north and south (timescale ~ 200 days). Some peter out or amalgamate with their neighbors and some are spontaneously generated. The Los Alamos Parallel Ocean Program (POP) model (Maltrud et al. 1998) displays similar behavior and will be compared with FRAM in section 4.

The formation of multiple jets in models of the ACC is reminiscent of results obtained by Rhines (1975), Williams (1978, applications to gas giant planets), and Pannetta (1993, applications to atmospheric jets) using quasigeostrophic models, which indicate that jet structure can arise from eddy–mean flow interaction. Rhines (1975) investigated the behavior of freely decaying turbulence on a barotropic β plane. Observing that the inverse cascade of energy to low wavenumbers in the turbulent flow would be halted when the eddy spatial scale reaches the resonant Rossby wave scale, he argued that such a flow organizes itself into zonal jets on long timescales. This yields a meridional scale for the long-term mean flow:

$$k_c = \sqrt{\frac{\beta}{2U}}, \qquad \lambda_c = 2\pi/k_c, \qquad (1)$$

where k_c is the dominant meridional wavenumber (corresponding wavelength λ_c), β is the (linear) variation of Coriolis parameter with latitude, and U is a characteristic eddy velocity.

Using a quasigeostrophic model with an imposed spatially uniform vertical shear and domains many times larger than the Rossby radius, Pannetta (1993) obtained time-mean flows consisting of several zonal jets where the scale of meridional variation was governed by (1).

Subsequently, Treguier and Pannetta (1994) discovered that zonation can arise naturally in a wind-forced baroclinic quasigeostrophic model provided the meridional extent of the domain is sufficient and the wind stress is of adequate strength. Meridionally oriented ridges or random topography with a specified height spectrum disrupt the jet structure and change the dynamical regime to one where the flow is controlled by topographically generated standing eddies. Transient eddies arising from baroclinic instability of the mean flow are believed to be responsible for maintaining the zonation in flat-bottomed cases, although the mechanism whereby this is achieved is still unclear. Clearly, it is also important to establish the role of lateral boundaries in restricting the number and spacing of multiple jets.

In this paper we consider the effect of meridional gradients of bottom topography. A meridional gradient of topography can act as a physical analog of the β effect, for example, a linear topographic slope in the meridional (y) direction induces planetary waves in a similar manner to the β effect, with the role of β played by the (constant) topographic slope α, scaled by the Coriolis parameter f_0 divided by the total ocean depth H. Like the β effect, a meridional topographic gradient inhibits meridional movement of water and thus, we suggest, stabilizes any evolving jets and additionally may alter jet spacing by locally changing the Rhines scaling parameter. In baroclinic flow, or with topography that does not vary linearly with latitude, there is no exact analogy with the β effect, and it becomes necessary to use models to examine the extent to which meridional topographic gradients influence the stability and spacing of jets.

To put the preceding ideas in quantitative form, we incorporate the scaled topographic slope into the β parameter resulting in a modified parameter, β_t, and postulate a new meridional scale:

$$k_c \sim \sqrt{\frac{\beta_t}{2U}} \qquad (2)$$

for which β_t represents the sum of all physical processes, for example, baroclinicity, topography, and boundary effects: the simplest hypothesis is that it will depend on the topographic slope ($\beta_t = \beta + f_0\alpha/H$), or in the case of more complicated topography, some average of the slope. We shall refer to (2) as the topographically modified Rhines scaling. The validity of (2) will be examined for quasigeostrophic flow (sections 2 and 3) and the FRAM/POP solutions (section 4). The paper concludes with a discussion on the significance of the results (section 5).

2. The quasigeostrophic model

We begin with a process study of Rhines' scaling using a model that solves the quasigeostrophic equations in Cartesian coordinates on a β plane in a zonally oriented reentrant (periodic) channel of length L_x, width L_y, and depth H. Variable

bottom topography of height b above the bottom is included. The x, y, and z axes are oriented eastward, northward, and vertically upward, respectively. The flow is constrained by rigid boundaries to the north and south. It is forced by a zonal wind stress τ [$\tau_x = \tau_0 \sin(\pi y/L_y)$, $\tau_y = 0$], while dissipation is effected by a linear bottom friction law (friction coefficient ν) and a biharmonic lateral friction operator (friction coefficient A_6). In the vertical direction a modal formulation is employed (Flierl 1978); that is, the solution to the full quasigeostrophic potential vorticity equation is expressed as the weighted sum of a complete set of orthonormal functions $F_i(z)$. The equations are briefly reviewed below; see Flierl (1978) for a rigorous derivation and full discussion of the relationship between layer and modal models. Our choice of a modal model rather than the frequently used layer approach lets us test the robustness of multiple jet formation across various model formulations. Furthermore the modal formulation is the more consistent one to employ when more than two physical mechanisms are included (e.g., baroclinicity, wind forcing, nonlinearity, and bottom friction as in the present case). In the following, f_0 is the Coriolis parameter at a reference latitude θ_0 (=$2\Omega \sin\theta_0$, where Ω is the earth's rotation rate) and $N^2(z)$ is the stratification parameter [=$(-g/\bar{\rho_0})d\rho_0(z)/dz$, where g is the acceleration due to gravity, $\bar{\rho_0}$ the mean density, and $\rho_0(z)$ the background density field]. We first define the geostrophic velocity field in terms of the geostrophic streamfunction Ψ,

$$u(x,\ y,\ z,\ t) = -\Psi_y/f_0, \qquad v(x,\ y,\ z,\ t) = \Psi_x/f_0, \quad (3)$$

where

$$\Psi(x,\ y,\ z,\ t) = \sum_i \phi_i(x,\ y,\ t)F_i(z). \quad (4)$$

The functions $F_i(z)$ are defined by

$$\frac{d}{dz}\left(\frac{f_0^2}{N^2(z)}\right)\frac{dF_i(z)}{dz} = -\lambda_i F_i(z)$$

$$\left.\frac{dF_i(z)}{dz}\right|_{z=0} = \left.\frac{dF_i(z)}{dz}\right|_{z=-H} = 0. \quad (5)$$

For the purposes of the paper we employ only the barotropic [$i = 1$, $\lambda_1 = 0$, $F_1(z) = 1$] and baroclinic ($i = 2$) modes and consider the simplest situation when baroclinicity is present. Here $F_2(z)$ and λ_2 are derived numerically using $N^2(z) = N^2_0$ $\exp(2.8z/H)$ with $N_0 = 2 \times 10^{-3}$ s^{-1}. For the stratification considered, the internal Rossby radius, $(\lambda_2)^{-1/2}$, is 36 km.

The prognostic equation for each modal streamfunction ϕ_k is

$$\frac{\partial(\nabla^2 - \lambda_k)\phi_k}{\partial t} + \beta\frac{\partial\phi_k}{\partial x} + \frac{1}{f_0}\sum_{ij} J(\phi_i, (\nabla^2 - \lambda_j)\phi_j)\xi_{ijk}$$

$$= -A_6\nabla^6\phi_k + \frac{f_0^2}{H}F_k(0)\frac{1}{f_0\rho_0}\text{curl}_z\tau - \frac{f_0}{H}F_k(-H)\sum_i (J(\phi_i, b) + (\nu/2f_0)^{1/2}\nabla^2\phi_i)F_i(-H), \quad (6)$$

(Click the equation graphic to enlarge/reduce size)

where ∇^2, ∇^6 are Laplacian and biharmonic operators and J the Jacobian operator [$J(A,\ B) = (\partial A/\partial x)(\partial B/\partial y) - (\partial A/\partial y)(\partial B/\partial x)$]. The ξ_{ijk} are constants defined as $\xi_{ijk} = (1/H)\int_{-H}^{0} F_i(z)F_j(z)F_k(z)\ dz$. The appropriate boundary conditions are periodic in x and $\partial\phi_k/\partial x = \nabla^2\phi_k = \nabla^4\phi_k = 0$ on the rigid boundaries. Finally, additional area and line integrals are required to make the set of model equations consistent and solvable (McWilliams 1977; the present paper adapts these integrals for a modal model). The unchanging parameters of the model are listed in Table 1 ⊙.

The model equations were discretized for numerical solution using standard second-order centered differences in space on an Arakawa-C-type grid (Arakawa 1966). Nonlinear terms were formulated using an energy and enstrophy conserving Jacobian (Arakawa and Lamb 1977). In time a leapfrog scheme was employed with an occasional forward time step to avoid development of a computational mode (Richtmyer and Morton 1967). The time step was 1.5 h and the horizontal resolution 20 km, sufficient to resolve the internal Rossby radius.

Four useful diagnostics from the model are the finite difference analogs of kinetic energy per unit area for each mode

$$E_2(t) = \frac{1}{2}\overline{\rho_0}H \int \int (\nabla\phi_2)^2 \ dx \ dy/L_xL_y,$$

the total potential energy per unit area

$$P(t) = \frac{1}{2}\overline{\rho_0}H \int \int \lambda_2\phi_2^2 \ dx \ dy/L_xL_y,$$

and the mass transport

$$T(t) = H[\Phi_1(0, L_y, t) - \Phi_1(0, 0, t)].$$

In each of the experiments the model was spun up to a state of statistical equilibrium such that $E_1(t)$, $E_2(t)$, $P(t)$, and $T(t)$ began to fluctuate about mean values with no discernible trend and was then integrated for a further period (typically 12 model years) in order to obtain mean streamfunctions ($\overline{\Phi_1}$, $\overline{\Phi_2}$) and velocites by averaging over the integration period. By analogy with the above equations for instantaneous energy, mean-flow energies (denoted by $\overline{E_1}$, $\overline{E_2}$, $\overline{P}$) can be defined based on the mean streamfunctions. The difference between the instantaneous energy averaged over the integration and the mean-flow energy is defined as the eddy energy (denoted by E'_1, E'_2, P').

A total of 11 quasigeostrophic simulations were performed with different combinations of channel width and topographic configuration (Table 2 ⊙⊐). Generally, experiments were conducted with a channel width of 3000 km (~ 83 Rossby radii). Two experiments were conducted with channel widths of 1500 km (~ 42 Rossby radii) and 4500 km (~ 125 Rossby radii), respectively. The latter width is an extreme case and is physically at the limit of consistency with the β-plane approximation for the earth; therefore the results must be viewed with caution. However, it was useful to run the model with this channel width to ascertain the effects of boundaries in constraining the flow. Flat-bottomed runs ($b = 0$) in narrow and wide channels were conducted to provide reference solutions. Experiments were conducted with linear slopes of varying steepness ($\partial b/\partial y = \alpha$) and with zonally constant (i.e., not varying in x) ridges centered at the midpoint of the channel, the cross section being either Gaussian, $b = b_0 \exp[-(y - L_y/2)^2/a^2]$, or harmonic, $b = b_0(1 - \cos2\pi y/L_y)^2/4$, in shape with maximum height $b_0 = 750$ m. In the case of Gaussian topography the width a was given the value 150 km, providing a strong contrast to the harmonic case where the width is of the order of half-channel width. A zonally constant form for the bottom topography was used in order to isolate the response to the augmentation of the β effect from other physical processes such as topographic form drag and upstream/downstream influences that may play a role in jet splitting (Wolff et al. 1991; Treguier and Pannetta 1994).

Experiments F1, F2, and F3 demonstrate the $(\beta/2U)^{1/2}$ scaling for a flat-bottomed ocean; L1–L6 form a parameter study of the effect of linear meridional variation of topography on the flow structure, while T1 and T2 consider the more complicated Gaussian and harmonic topographic shapes.

The method of analysis was to calculate the meridional scale of variation of the flows from the time- and zonally averaged u-velocity profiles and compare them with the predicted scale from (2) using U obtained from the eddy kinetic energy for the simulation and β_t obtained from the topographic slope as discussed in section 1.

3. Results from the quasigeostrophic model

a. Flat-bottomed experiments

The flat-bottomed solution in a relatively narrow channel, F1, is well known from the research of such authors as McWilliams et al. (1978), McWilliams and Chow (1981), Treguier and McWilliams (1990), and Wolff et al. (1991). The statistically equilibrated solution consists of an intense and narrow meandering central jet flanked by mesoscale eddies. The equilibrated solution of the wider channel, F2, behaves differently. Figure 3 ⊙⊐ depicts the instantaneous surface streamfunction after 24 model years of integration. Clearly, at this point in time the wider channel exhibits three jet structures side by side instead of one. Time series of kinetic and potential energies and mass transport for the flat-bottomed experiment, F2, are displayed in Fig. 4 ⊙⊐. The solution F2 was similar to F1 in terms of kinetic energy levels but displayed larger values for the potential energy and mass transport reflecting the larger domain size. Hovmöller diagrams were constructed for each experiment by contouring the surface u velocity along the meridional line $x = 960$ km against time. The extended domain of F2 allows a complex jet structure to develop with two–three jets present at any one time (Fig. 5 ⊙⊐). Jets arise spontaneously at the edges of the domain, meander, and on occasion coalesce with neighbors. In the zonally constant case there is no preferred location in the channel, and hence the long-term mean solution is also zonally constant. The differences in the characteristics of the mean flow structures between the solutions can be demonstrated by means of a comparison of the time- and zonally averaged u-velocity profiles across the channel (Fig. 6a ⊙⊐). The F1 experiment is dominated by a single jet in the center of the channel flanked (in the upper layer) by two "shoulders," perhaps the precursors

of further jets not fully developed due to the restricted latitudinal extent of the model. In F2 there are two jets of equal strength appearing in the wider channel, demonstrating clearly that the strength of the wind stress is no indication of the positions of the jets. The position of maximum wind stress (the center of the channel) is the location of a local minimum of the mean zonal velocity profile. The flow also exhibits smaller maxima between the main jets hinting at the emergence of additional jets, given even greater latitudinal extent. However the Hovmöller diagram for this experiment demonstrates that the time-dependent behavior is more complex than would appear from the velocity profile alone. The latitudinal extent of the model was extended even farther in F3 to 4500 km. The mean zonal velocity shows a four-jet structure.

The domain-averaged mean-flow kinetic, eddy kinetic, mean-flow potential, and eddy potential energies and the mean mass transport calculated during the statistically equilibrated periods of the quasigeostrophic experiments are tabulated in Table 3 ⚬. Considering the flat-bottomed experiments, the mean mass transport shows a simple linear trend between the three runs, rows 1–3. The levels of mean-flow energy vary widely over the three runs, while the levels of eddy energy are remarkably similar. Clearly, the change in mean-flow potential energy can be attributed to the increase in domain width from F1 to F3. The reason for the disparities in kinetic energy are not as easy to explain. The mean-flow kinetic energies of F1 and F2 are quite similar, whereas the ratio of eddy kinetic energy to mean-flow kinetic energy rises from 28% in F1 to 43% in F2. Moreover, this rise is manifested entirely in the energy associated with the barotropic mode. Here F3 sees a dramatic rise in the mean-flow kinetic energy associated with both barotropic and baroclinic modes, but the absolute values of the eddy kinetic energies are similar to F1, the ratio of eddy to mean-flow kinetic energy being therefore dramatically reduced to only 6%. Note that the experimental conditions are not exactly identical as the length scale of the forcing increases with the width of the channel with a concomitant increase in the energy input. Also the influence of the rigid lateral boundaries on the central regions of the model diminishes as the channel length increases.

The observed meridional scale of the variation of the velocity, λ_{obs}, is about 760 km for F1, 820 km for F2, and 800 km for F3 (Table 4 ⚬, first three rows). These are taken to be average peak-to-peak (excluding the smaller maxima and boundary layers) or minimum-to-minimum distances measured directly off the mean zonal velocity plots (Pannetta 1993). The value of the characteristic velocity U is evaluated from the eddy kinetic energy according to the formula

$$U = (2E'_1)^{1/2}. \quad (7)$$

Due to its dominance in the energetics only the energy associated with the barotropic mode is used to calculate the Rhines scaling. Generally speaking, the eddy energy associated with the baroclinic mode is <20% of that associated with the barotropic mode in all the quasigeostrophic experiments and, therefore, would only change the Rhines scaling estimates by less than 10%. Here U is 12.9 cm s^{-1} for F1, 15.1 cm s^{-1} for F2, and 14.0 cm s^{-1} for F3. Since β_t in this case is simply β ($=1.4 \times 10^{-11}$ s^{-1}), the expected meridional scale λ_c based on the Rhines arguments calculated according to (2), results in 830 km for F1 and 900 km for F2 and 870 km for F3. It will be seen that for the flat-bottomed experiments the Rhines scaling gives the right order of magnitude for the jet spacing. However, it is clear that the observed length scales are consistently lower than those predicted by about 10%. One possible reason is the effect of the boundaries. Figure 6 ⚬ shows that this is substantial even in very wide channels, the influence being felt over the order of perhaps 500 km from each boundary, and may extend to altering the Rhines scaling on the peripheries of the model domain, pushing the evolving jets closer together. As will be seen in the next subsection the Rhines scaling does lead to a slight overestimate of the observed length scale in the other quasigeostrophic experiments (and indeed in the GCMs, section 4).

b. Linear topography

The analogy between meridional gradient of topography and the β effect is not absolute in a baroclinic system. The last term in (6) indicates that the interaction of the bottom with the baroclinic mode can affect the barotropic flow and vice versa. The importance of these interactions has not yet been studied, and therefore we perform a baseline series of runs in a channel 3000 km wide using linearly varying topography of different slopes in order to establish how the jet scaling varies in this very simple system. It is clear from the equations of motion that, if the depth of the ocean decreases on going from south to north, this will result in an effective decrease in the β parameter. We address the extent of the increase and whether this can be expressed simply by adding the scaled topographic slope to β. Table 2 ⚬ lists the changing bottom slope from L1 to L6. Negative (positive) slope indicates shallower (deeper) water on the southern side, augmenting (reducing) β. The series begins with L1 (maximum positive slope) and ends with L6 (maximum negative slope); F2 (zero slope) fits between L3 and L4.

The seven experiments form a useful parameter study, and trends can be seen in the bulk parameters that characterize the flow (Table 3 ⚬). There appear to be two regimes: The first consists of positive and zero slopes (L1–F2) where the kinetic energy of both mean flow and eddies increases linearly with decreasing slope (for the barotropic mode, which contains most of the energy, about 30% increase in mean-flow kinetic energy from L1 to F2 and 50% increase in eddy kinetic energy over the same parameter range). The second regime consists of negative slopes where the kinetic energy of the mean flow is dramatically increased (by a factor of >4 for the barotropic mode between F2 and L4) while the eddy kinetic energy stagnates (4% change between F2 and L6 for the barotropic mode). The mean-flow potential energy rises steadily from L1 to L6, the extremes differing by a factor of 7. The eddy potential energy varied little (<20%) over the parameter range. The mean mass transport showed a steadily increasing linear trend.

The most important features of the solutions from the point of view of the present study is the number and spacing of the jets. These show a regular pattern (Fig. 6b ⚬). For the most positive value of bottom slope (L1) there is no discernible jet

and the velocity structure reflects the pattern of the wind stress. Clearly, with β effectively zero the Reynolds stresses no longer concentrate momentum, and the flow is diffuse. As the bottom slope becomes less positive and reaches zero (L2–F2), two jets are in evidence; the spacing decreasing only slowly. However, the number of smaller maxima increases with decreasing positive slope. Note that the number of jets jumps directly from zero to two: we were unable to locate a solution with only one distinct jet in a channel 3000 km wide. As the bottom slope decreases further to negative values (L4–L6), three jets occur, the spacing decreases slowly, and with L6 smaller maxima are apparent, probably presaging the appearance of an additional jet if the topographic slope is decreased further. It should be emphasized once again that the mean zonal velocity profile presents a simplified picture of the flow and the number of jets. The corresponding Hovmöller diagrams (not shown) indicate that jet formation, annihilation, and coalescence occurs throughout the experiments, and there are significant periods where the number of jets is higher or lower than the average value recorded based on the mean zonal velocity profile. The predicted jet spacing, λ_c, for these runs is of the right order of magnitude and shows the correct trends (Table 4 ⊙▬). The precise values are 10%–20% greater than those observed. Other effects are involved in the jet spacing, probably in addition to any boundary effects discussed for flat-bottomed experiments, as the overprediction is slightly greater in the topographic cases. It is likely that the topography enhances β slightly more than expected (by $\sim 20\%$) due to the interaction of the baroclinic mode with topography.

c. Gaussian and harmonic hills

The preceding section has demonstrated that linear slopes fit fairly well within the framework of the Rhines scaling arguments (with the reservations already noted and with a small systematic error). We now move to cases with more complicated topography (though still zonally constant). The more complex behavior that can arise is illustrated by two simulations (T1 and T2) using ridges of Gaussian and harmonic cross sections (section 2), respectively (Fig. 6c ⊙▬). The harmonic ridge produces a solution with approximately double the mean-flow kinetic energy of the Gaussian ridge but with less potential energy (Table 3 ⊙▬). The eddy energy levels are similar in both cases, and the mean mass transports are not significantly different. On average, there are two jets in each case. The wider topography results in the flow being enhanced (depressed) on the northern (southern) side of the ridge where the topography is enhancing (reducing) β. For the narrower topography the southern jet is entirely to the south of the topography, while the northern jet is positioned directly above the topography in a position where β is being most effectively increased by the negative sign of the topographic slope. Evidently, when the topography varies on sufficiently small length scales, the flow is not able to adjust on the same scale. In the case of variation on a large length scale the flow is able to adjust according to the local topographic slope. For the Gaussian hill the mean topographic slope in a direction enhancing β is of order $2b_0/H$, while for the harmonic ridge it is of order b_0/H. These are the values used to calculate β_t in Table 4 ⊙▬. Both provide useful predictions of the jet scaling in these cases.

It will be seen that there is general agreement between the quasigeostrophic experiments and theory. In section 4 we see if this holds in the more complicated domain of a GCM.

d. Roughness effects

The preceding sections have dealt with idealized strongly barotropic flows where the transport is very high compared to that observed in nature. To test the relevance for real flows with a stronger baroclinic component, we have conducted quasigeostrophic experiments with bottom roughness in addition to large-scale slopes. The detailed results from these experiments will be discussed elsewhere. However, the results from a simulation ($L_x = 4000$ km, $L_y = 3000$ km) with random topography (rms height 200 m) with an isotropic Gaussian wavenumber spectrum with random phases of bandwidth ($2\pi/400$ km) and centered on wavenumber ($2\pi/250$ km) showed a similar mean zonal velocity profile to the flat-bottomed case (i.e., similar to Fig. 6a ⊙▬ but with reduced velocities). Similarly, when the random topography was superimposed on a large-scale negative slope, the depressing effect on β was preserved although the mean mass transport was reduced.

4. FRAM and POP results

The results from two ocean GCMs have been analyzed, FRAM (FRAM Group 1991) and POP (Maltrud et al. 1998). The model configurations differ in a number of aspects. Here we detail those aspects that are most relevant to our study. FRAM has a horizontal resolution of approximately 28 km with a domain from the Antarctic coast to 24°S. The topography has been smoothed and the ocean forced by seasonal winds and a constant buoyancy term. POP, on the other hand, is almost global in extent, reaching to 78°N. It uses a Mercator grid that has a resolution of approximately 16 km at 60°S and unsmoothed topography. The forcing is by three-day averages of ECMWF winds and a seasonal heat flux.

FRAM generally possesses less eddy energy than quasigeostrophic models (cf. Kruse et al. 1990). The region of large mean currents is confined to a band of width 20°–25° latitude, though the band is centered on different latitudes in the various regions. The multiple jet structure is superimposed on a large-scale shear that varies on a length scale of >1000 km. The Hovmöller diagram (Fig. 2 ⊙▬) shows that the flow consists of a number of jets meandering to the north and south over time. The velocity filaments remain well correlated over fairly large longitudinal ranges (typically 30° of longitude ~ 1600 km at the latitude of the ACC).

The main topographic features along the track of the ACC are the midocean ridge systems, Kerguelan Island, and the Crozet Plateau. We consider three regions in the Indian Ocean and West and East Pacific Ocean (designated with a single letter a–c), respectively, where the bottom topography is relatively zonal (Table 5 ⊙▬). The topography and the time-mean

near-surface (32.5 m for FRAM, 12.5 m for POP) u velocity (based on the last five years of integration for both FRAM and POP) were longitude-averaged over the ranges (typically 30°–40°) specified in Table 5 ⊙ (Figs. 7 ⊙ and 8 ⊙). In the cases selected a single more-or-less zonally oriented hill or slope dominates the bottom relief. The smoothed, slightly shallower topography in FRAM contrasts with the rougher, slightly deeper topography of POP. It should be noted that the large-scale zonal averaging tends to smooth out the velocity field. In addition to eddy–mean flow interaction the shape of the mean velocity profile will be affected by other factors such as topographic steering. It is hoped that these other effects will be small due to the relatively small departures of the topography from zonality.

We first consider Fig. 7 ⊙ in detail. In case a, the mean flow is enhanced over a topographic ridge of height approximately 1000 m centered at about 50°S and of total width about 20° of latitude. This ridge is bounded to the north and south by very steeply varying topography that effectively confines the mean flow to the region above the ridge. On the north side of the ridge the topography is in such a direction as to enhance the planetary vorticity gradient, while on the south side there should be a weakening of the β effect, a situation analogous to the quasigeostrophic simulation T2. Observation of the velocity field above shows more structure on the south side of the ridge than on the north. Case b is dominated by depth increasing in the south–north direction, over which most of the mean flow is located, and would thus be expected to enhance the β effect. The flow above the topography is dominated by fairly broadscale jets, although there is smaller-scale variation that splits the tips of the jets. Finally, in case c the main topographic feature exhibits depth increasing in the southward direction, opposing the β effect. However, in all cases there is a region of steep topography to the extreme south oriented to strongly enhance β. Note that typical velocities in all regions are of order 10 cm s^{-1} (the range is 7.5–12.5 cm s^{-1})—much smaller than the equivalent quasigeostrophic experiments.

The POP model (Fig. 8 ⊙) produces multiple jets similar to FRAM, an interesting result in itself given the differences in model configuration, although the magnitudes of the mean velocities are slightly larger, typical peak velocities being about 15 cm s^{-1}, and the length scales are clearly smaller in general. Also the regions of strongest mean currents differ from those in FRAM. In case a there is a clearly defined difference in flow on each side of the ridge with multiple jets being confined to the southern side. The jet structure is much more pronounced than in FRAM. Case b shows multiple jet structure over a similar region to the FRAM model; however as already noted, the length scale of the jets appears to be smaller. Case c shows well-developed jet structure over the major topographic slope centered at about 55°S with two distinct length scales: broader (narrower) to the north (south) of 65°S.

As in the quasigeostrophic case we redefine the variation in background potential vorticity gradient to include topographic effects [Eq. (2)]. As two estimates of β_t we choose the mean and rms values across the domain (calculated for latitudes south of 40°S since this is the region of strong flow in all three cases) of the effective β [$\beta + f_0(\partial b/\partial y)/H$]. The values of U are obtained from the average near-surface eddy energy in each of the three regions over the final five years of both FRAM and POP simulations. Here U is of order 5–7 cm s^{-1} for FRAM and 12 cm s^{-1} for POP, well below the quasigeostrophic results. The observed meridional scale is much harder to judge by eye for the FRAM and POP results than for the quasigeostrophic results due to the presence of a broadscale flow on which the multiple jets are superimposed. In order to remove this feature each u-velocity profile in Figs. 7 ⊙ and 8 ⊙ was filtered using a running mean (51-point for FRAM and 61-point for POP equivalent to averaging on scales of $\sim$ 1500 km) and the result subtracted from the original profile to highlight the multiple jet structure. The midpoints of successive zero-crossings were taken as the centers of the jets allowing the number and average spacing of the jets to be calculated (Fig. 9 ⊙). We restrict ourselves to latitudes south of 40°S as explained above. It is useful to invert Eqs. (1) and (2) in order to derive the effective β required to produce the observed scale of variation

$$\beta_e = \frac{8\pi^2 U}{\lambda_{obs}^2}. \qquad (8)$$

Tables 6 ⊙ (FRAM) and 7 ⊙ (POP) display values of observed wavelength, λ_{obs}, U, β_e, and the number of jets followed by the two estimates of β_t and the corresponding estimates of the Rhines scaling λ_c. In the case of FRAM there is excellent agreement ($\sim$ 10% error) between observed and predicted length scales with the mean and rms providing high and low estimates, respectively. The results from POP present a much less consistent picture. Case a shows the best agreement with similar accuracy to FRAM. On the other hand, case b exhibits very short length scales ($\sim$ 50% of the calculated values) and the Rhines scaling cannot be of major importance in determining this scale. Case c is an intermediate case. The presence of rough topography in the POP model supports the possibility that topographic control by standing eddies (Treguier and Pannetta 1994) is of greater importance compared with FRAM.

5. Conclusions

The various models with differing physics, resolution, and forcing considered in this study all produce a multiple jet flow and indicate that the presence of zonal jets is a robust feature of Southern Ocean–like flows. We have demonstrated that a major factor controlling the scaling of the jets in quasigeostrophic flow is the β effect coupled with eddy–mean flow interaction. In a zonal channel configuration the stratified flow has a strong barotropic component and hence "feels" the bottom. The effective β restricting the meridional extent of the flow is thus a function of the topography. While it is possible to confidently predict the scaling arising in flat-bottomed cases or cases with linearly varying topography, the effects of more complicated topography, although conforming to the same general principles, cannot necessarily be predicted in advance with accuracy. Preliminary simulations with bottom roughness present indicate that for roughness on certain scales

at least, the large-scale meridional slope rather than the roughness still determines the meridional scaling [but Treguier and Pannetta (1994) show that other scales of roughness may have more radical effects]. Clearly, our understanding of the effects of rough topography would benefit from a detailed parameter study.

Despite their many differences in configuration, the ocean GCMs FRAM and POP produce a very similar streaky, jetlike flow. There is reasonable agreement between the observed length scales and the topographically adjusted Rhines scaling in all three regimes studied in FRAM and in one to two out of three regimes studied in POP. Because both FRAM and POP possess similar amounts of eddy energy, there is no great difference in the jet spacing observed between these cases (the range is 250–500 km). There is no agreement with the topographically adjusted Rhines scaling in one of the regimes studied in POP, and it is likely that other effects are of importance in determining the jet structure, in particular topographic control by standing eddies generated from nonzonal topography as in Treguier and Pannetta (1994). In support of this, it is important to note that the POP bathymetry is significantly rougher than that in FRAM.

That the ACC consists of multiple jets or current cores of fairly limited meridional scale is well known. The present study quantifies the expected scale of variation of the jet structure and highlights the factors determining both the scaling and the location of the multiple jets relative to the large-scale topography. Further studies are required to investigate the effects of isolated topographic features and smaller-scale roughness on the structure of the flow. It would also be of interest to make comparisons with zonal or near-zonal current systems, for example, the Azores Current (eastern North Atlantic, $\sim 34°$N; see Pingree 1998).

REFERENCES

Arakawa, A., 1966: Computational design for long term numerical integration of the equations of fluid motion: Two-dimensional incompressible flow. Part I. *J. Comput. Phys.,* **1,** 119–143..

—— ,and V. R. Lamb, 1977: Computational design of the basic dynamical processes of the UCLA general circulation model. *Meth. Comput. Phys.,* **17,** 173–265..

Flierl, G. R., 1978: Models of vertical structure and the calibration of two-layer models. *Dyn. Atmos. Oceans,* **2,** 341–381..

FRAM Group, 1991: An eddy resolving model of the Southern Ocean. *Eos, Trans. Amer. Geophys. Union,* **72** (15), 169, 174–175..

Hofmann, E. E., 1985: The large-scale structure of the Antarctic Circumpolar Current from FGGE drifters. *J. Geophys. Res.,* **90,** 7087–7097..

Kruse, F., A. Hense, D. Olbers, and J. Schröter, 1990: A quasigeostrophic eddy-resolving model of the Antarctic Circumpolar Current: A description of the model and the first experiment. Alfred-Wegener Institut für Polar- und Meeresforschung Tech. Rep., 62 pp. [Available from Alfred-Wegener Institut für Polar- und Meeresforschung, Am Handelshafen 12, D-2850 Bremerhaven, Germany.].

Maltrud, M. E., R. D. Smith, A. J. Semtner, and R. C. Malone, 1998:Global eddy-resolving ocean simulations driven by 1985–94 atmospheric fields. *J. Geophys. Res.,* **103** (C13), 30 825–30 853..

McWilliams, J. C., 1977: A note on a consistent quasigeostrophic model in a multiply connected domain. *Dyn. Atmos. Oceans,* **1,** 427–441..

—— ,and J. H. S. Chow, 1981: Equilibrium geostrophic turbulence. I: A reference solution in a β-plane channel. *J. Phys. Oceanogr.,* **11,** 921–949.. Find this article online

—— ,W. R. Holland, and J. H. S. Chow, 1978: A description of numerical Antarctic Circumpolar Currents. *Dyn. Atmos. Oceans,* **2,** 213–291..

Nowlin, W. D., Jr., and M. Clifford, 1982: The kinematic and thermohaline zonation of the Antarctic Circumpolar Current at Drake Passage. *J. Mar. Res.,* **40** (Suppl.), 481–507..

—— ,and J. M. Klinck, 1986: The physics of the Antarctic Circumpolar Current. *Rev. Geophys.,* **24,** 469–491..

Orsi, A. H., T. Whitworth III, and W. D. Nowlin, 1995: On the meridional extent and fronts of the Antarctic Circumpolar Current. *Deep-Sea Res. I,* **42** (5), 641–673..

Pannetta, R. L., 1993: Zonal jets in wide baroclinically unstable regions: Persistence and scale selection. *J. Atmos. Sci.,* **50,** 2073–2106.. Find this article online

Pingree, R. D., 1998: The eastern subtropical gyre (North Atlantic):Flow rings recirculation structure and subduction. *J. Mar. Biol. Assoc. U.K.,* **77,** 573–626..

Rhines, P. B., 1975: Waves and turbulence on a β-plane. *J. Fluid Mech.,* **69,** 417–443..

Richtmyer, R. D., and K. W. Morton, 1967: *Difference Methods for Initial-Value Problems.* 2d ed. J. Wiley and Sons..

Treguier, A. M., and J. C. McWilliams, 1990: Topographic influence on wind-driven stratified flow in a β-plane channel—An idealized model of the Antarctic Circumpolar Current. *J. Phys. Oceanogr.,* **20,** 321–343.. Find this article online

— , and R. L. Pannetta, 1994: Multiple zonal jets in a quasigeostrophic model of the Antarctic Circumpolar Current. *J. Phys. Oceanogr.,* **24,** 2263–2277.. Find this article online

Williams, G. P., 1978: Planetary circulations: I. Barotropic representations of Jovian and terrestrial turbulence. *J. Atmos. Sci.,* **35,** 1399–1426.. Find this article online

Wolff, J.-O., E. Maier-Reimer, and D. J. Olbers, 1991: Wind-driven flow over topography in a zonal β-plane channel: A quasi-geostrophic model of the Antarctic Circumpolar Current. *J. Phys. Oceanogr.,* **21,** 236–264.. Find this article online

Tables

Table 1. Basic parameters of the quasigeostrophic model.

Parameter	Value
H/m	5000
τ_0 (N m^{-2})	0.1
ε (s^{-1})	10^{-7}
A_4 (m^4 s^{-1})	10^{10}
L_x (km)	1920
θ_0 (deg)	50.0
f_0 (s^{-1})	-1.1×10^{-4}
β (m^{-1} s^{-1})	1.5×10^{-11}

Click on thumbnail for full-sized image.

Table 2. Description of quasigeostrophic simulations.

Model	L_y (km)	Type of topography
F1	1500	None
F2	3000	None
F3	4500	None
L1	3000	Linear, $\alpha = 5.0 \times 10^{-4}$
L2	3000	Linear, $\alpha = 3.3 \times 10^{-4}$
L3	3000	Linear, $\alpha = 1.7 \times 10^{-4}$
L4	3000	Linear, $\alpha = -1.7 \times 10^{-4}$
L5	3000	Linear, $\alpha = -3.3 \times 10^{-4}$
L6	3000	Linear, $\alpha = -5.0 \times 10^{-4}$
T1	3000	Gaussian, see text
T2	3000	Harmonic, see text

Click on thumbnail for full-sized image.

Table 3. Energetics of quasigeostrophic simulations (symbols defined in the text, energies in kJ m^{-2}, transport in Sv).

Model	$\overline{E}_1$	$\overline{E}_2$	$\overline{P}$	E'_1	E'_2	P'	T
F1	144.8	12.5	754	41.7	11.2	37	1252
F2	130.0	15.2	2748	57.0	11.9	36	2502
F3	769.2	160.3	5911	48.8	11.6	32	3788
L1	101.3	6.3	774	34.3	11.7	37	2240
L2	111.9	8.7	1234	39.7	11.7	37	2314
L3	120.1	11.3	1897	48.8	12.1	38	2402
L4	507.7	114.8	3648	56.7	11.9	33	2571
L5	768.1	198.0	4669	59.5	14.1	33	2756
L6	724.3	201.9	5507	56.7	14.8	40	2805
T1	154.6	20.6	4858	41.0	12.9	32	2635
T2	278.9	57.9	3479	51.1	12.1	36	2571

Click on thumbnail for full-sized image.

Table 4. Results from quasigeostrophic simulations.

Model	Number of distinct jets	λ_{obs} (km)	U (m s^{-1})	β_t (10^{-11} m^{-1} s^{-1})	λ_c (km)
F1	1	>750	0.129	1.47	830
F2	2	820	0.151	1.47	900
F3	4	800	0.140	1.47	870
L1	0	—	0.117	0.36	1600
L2	2	850	0.126	0.73	1170
L3	2	850	0.140	1.10	1000
L4	3	700	0.151	1.84	800
L5	3	700	0.154	2.21	740
L6	3	550	0.151	2.58	680
T1	2	590	0.128	2.58	660
T2	2	800	0.143	2.03	750

Click on thumbnail for full-sized image.

Table 5. Regions analyzed (FRAM and POP models).

Click on thumbnail for full-sized image.

Table 6. Results from FRAM.

Case	Jets	A_{inc} (km)	U (cm s^{-1})	β_o (10^{-11} m^{-1} s^{-1})	β_c (10^{-11} m^{-1} s^{-1}) Mean	rms	A_c (km) Mean	rms
a	7	390	5.6	2.91	2.69	3.89	405	340
b	7	450	7.0	2.73	2.44	3.45	475	400
c	7	490	5.8	1.91	2.16	3.46	460	360

Click on thumbnail for full-sized image.

Table 7. Results from POP.

Case	Jets	A_{inc} (km)	U (cm s^{-1})	β_o (10^{-11} m^{-1} s^{-1})	β_c (10^{-11} m^{-1} s^{-1}) Mean	rms	A_c (km) Mean	rms
a	6	445	11.9	4.75	3.55	5.97	515	400
b	10	260	11.7	13.67	3.44	6.46	520	380
c	9	350	11.9	7.67	3.20	5.78	540	400

Click on thumbnail for full-sized image.

Figures

Click on thumbnail for full-sized image.

Fig. 1. Depth–latitude diagram at 270°E showing depth coherence of FRAM u velocity. Contours are in centimeters per second.
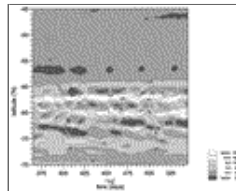
Click on thumbnail for full-sized image.

Fig. 2. Hovmöller diagrams [near-surface (32.5 m) u velocity in cm s^{-1} contoured in time vs latitude] showing temporal coherence of FRAM jets at 270°E.
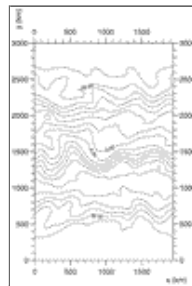
Click on thumbnail for full-sized image.

Fig. 3. Typical instantaneous surface streamfunction divided by f_0, quasigeostrophic model, case F2. Contours are in m^2 s^{-1}.
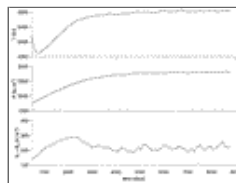
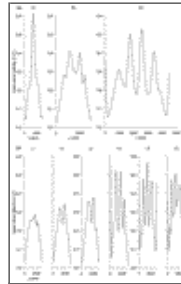Click on thumbnail for full-sized image.

Fig. 4. Spinup characteristics for quasigeostrophic model, case F2. Top: mass transport, center: potential energy per unit area, and bottom: total kinetic energy per unit area.
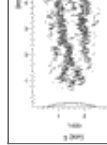
Fig. 5. Hovmöller diagram for run F2 showing instantaneous zonal velocity as a function of meridional distance and time at $x = 960$ km. For clarity, only the 1 m s^{-1} contour is shown.

Fig. 6. Surface zonal velocity profiles (quasigeostrophic model) averaged over equilibrium period T and over channel length L_x. For (a) cases F1, F2, and F3; (b) cases L1–L6; and (c) cases T1 and T2. The underlying topographic variation is shown as a dotted line. Maximum topographic
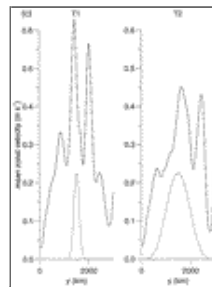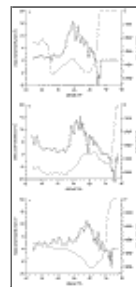
Fig. 6. (*Continued*) height is 750 m in both cases. Velocity scale runs from 0 to 0.6 m s^{-1} in all cases. See Table 2 for channel widths.
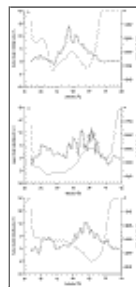
Fig. 7. Longitude-averaged time mean near-surface (32.5 m) u velocity from the FRAM model for (a) 85°–135°E, (b) 190°–225°E, and (c) 240°–280°E. The underlying (longitude averaged) topographic variation is shown as a dotted line.

Fig. 8. As in Fig. 7 but for the POP model.
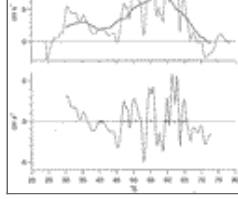
Fig. 9. Calculation of number and spacing of multiple jets in FRAM and POP. The example given is case c of FRAM. Top panel: longitude-averaged time mean near-surface (32.5 m) u velocity (thin line) and results of filtering with a 51-point running mean (thick line). Bottom panel: Difference between the two curves in the top panel. Dots show the zero crossings of the curve. Crosses denote the jet centers. The number of jets (Tables 6 ⊙ and 7 ⊙) is given by the number of crosses, while the jet spacing is given by the mean separation of the crosses.

Corresponding author address: Dr. Bablu Sinha, Plymouth Marine Laboratory, Citadel Hill, Plymouth PL1 2PB, United Kingdom.

E-mail: bs@pml.ac.uk

top ▲